Direct Observations of a Dynamically Driven Phase Transition with *in situ* X-Ray Diffraction in a Simple Ionic Crystal

Patricia Kalita,* Paul Specht, and Seth Root
Sandia National Laboratories, Albuquerque, New Mexico 87125, USA

Nicholas Sinclair and Adam Schuman
Dynamic Compression Sector, Institute for Shock Physics, Washington State University, Argonne, Illinois 60439, USA

Melanie White and Andrew L. Cornelius
High Pressure Science and Engineering Center, University of Nevada Las Vegas, Las Vegas, Nevada 89154, USA

Jesse Smith and Stanislav Sinogeikin
High-Pressure Collaborative Access Team, Carnegie Institution of Washington, Argonne, Illinois 60439, USA
(Received 15 July 2017; revised manuscript received 16 October 2017; published 21 December 2017)

We report real-time observations of a phase transition in the ionic solid CaF_2, a model AB_2 structure in high-pressure physics. Synchrotron x-ray diffraction coupled with dynamic loading to 27.7 GPa, and separately with static compression, follows, *in situ*, the fluorite to cotunnite structural phase transition, both on nanosecond and on minute time scales. Using Rietveld refinement techniques, we examine the kinetics and hysteresis of the transition. Our results give insight into the kinetic time scale of the fluorite-cotunnite phase transition under shock compression, which is relevant to a number of isomorphic compounds.

DOI: 10.1103/PhysRevLett.119.255701

Understanding the behavior of compression-driven phase transformations, their pathways, and kinetics, lies at the core of contemporary static and dynamic compression research at advanced light sources [1]. Traditionally, shock compression research infers phase transitions from continuum-level measurements and uses corresponding static compression experiments, shock-recovery studies, or calculations to deduce the resulting phase. The advent of synchrotron facilities where shock compression is coupled with real-time x-ray diffraction (XRD) now allows for microstructural identification of phase transitions and monitoring of transition kinetics [2–4]. Prior dynamic diffraction experimental work has focused on melting, crystallization, and the solid-solid phase transition in a simple monoatomic solid. Here, we present direct observation of the complex solid-solid phase transition in an AB_2 ionic crystal, CaF_2.

Somewhat surprisingly, given the relative simplicity of CaF_2 and the many high-pressure studies [5–11], little data is available from dynamic compression. Upon static compression to 9 GPa (hydrostatic) or 11–16 GPa (nonhydrostatic), CaF_2 undergoes a phase transition from the cubic fluorite structure ($Fm\bar{3}m$, $Z = 4$) to an orthorhombic cotunnite-type structure ($Pnam$, $Z = 4$) [7,12,13]. The sensitivity to nonhydrostatic conditions on static compression suggests a sensitivity to dynamic compression.

Early shock compression experiments reported observing the cotunnite phase of CaF_2 using x-ray diffraction on recovered samples [14,15]. More recently, researchers made real-time measurements on CaF_2 using continuum-scale velocimetry that suggested the presence of a phase transition under shock [16,17]. However, these measurements do not provide time-resolved lattice or structure information. The transition observed in the velocimetry data was assumed to be fluorite to cotunnite, analogous to static compression studies.

In this Letter, we report the method and results from the first direct, real-time, microstructural, atomic-scale observations of a shock-driven phase transition in CaF_2. Synchrotron XRD experiments are coupled with plate impact launchers and photonic Doppler velocimetry (PDV) to follow, *in situ*, the solid-solid phase transition in shock-compressed CaF_2. The results are compared with our XRD studies under static compression and high temperatures, designed to mimic the states achieved in shock compression. We discuss the kinetics and the reversibility of the transition both qualitatively and quantitatively. Finally we present Hugoniot equation-of-state data for 75% dense porous CaF_2.

Plate-impact shock wave experiments coupled with dynamic XRD were performed on CaF_2 powder compacts. Lexan® flyer plates were accelerated from 2 to 6 km/s using a two-stage light gas gun or powder gun that impacted finely ground CaF_2 powders $\sim 75\% \pm 1\%$ theoretical maximum density (TMD), single crystal $\rho_0 = 3.18$ g/cm^3. The back surface of each sample was mounted to a TPX® window [18,19]. Experiments were performed at the Dynamic Compression Sector at the Advanced Photon Source. A focused pink x-ray beam is used for single-pulse XRD images (~100-ps duration). A four-image XRD detector allows for the study of temporal evolution of structure during shock compression by recording four XRD snapshots [20].

Figure 1, inset, shows a schematic view of the experimental configuration. The Lexan projectile impacts CaF_2, sending a shock wave through the sample. A four-channel PDV system

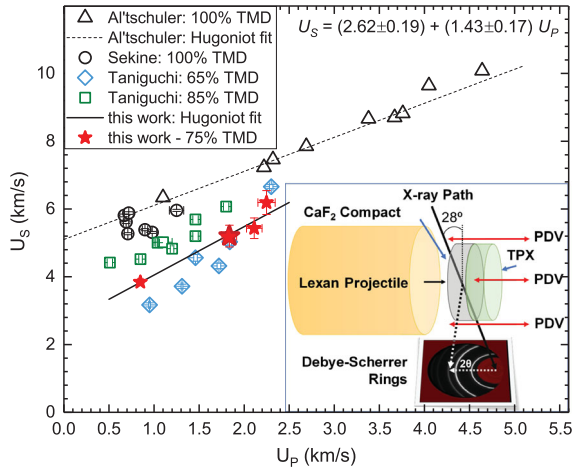

FIG. 1. Experimental Hugoniot data in the shock velocity (U_S) versus particle velocity (U_P) plane, for five shots (two data points are overlapped). Five solid red stars (two are overlapped) represent CaF_2 at 75% ± 1% TMD investigated in this work. Open symbols refer to literature data for CaF_2 at various initial densities [17,32,33].

[21] records the impact time and the particle velocity (U_P) at the CaF_2-TPX interface. The first abrupt change in the interface U_P indicates the initial shock arrival time at the CaF_2-TPX interface (Fig. 2). The shock velocity is calculated from the known thickness and shock wave transit time. Using the Lexan Hugoniot data [18] along with the measured impact velocity, we apply the Rankine-Hugoniot jump conditions [31] and the Monte Carlo impedance matching [20,22] method, to determine the CaF_2 density (ρ), stress (σ), and U_P. The resulting Hugoniot states are plotted in U_S-U_P space in Fig. 1. A linear fit to our data yields $U_S = (2.62 \pm 0.19) + (1.43 \pm 0.17)U_P$ with a covariance of −0.030994 between

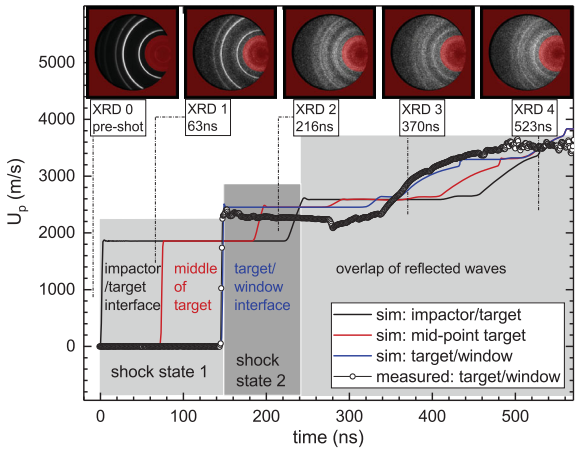

FIG. 2. Example of the temporal connection between XRD images acquired and the evolution of the shock event as measured by PDV (circles). Dashed lines show times when Debye-Scherrer rings were recorded (corresponding diffraction shown in Fig. 3). Simulated U_P traces (solid lines, using the Hugoniot data of Ref. [33]) illustrate the shock state of the sample at three locations.

the parameters. Comparison with Ref. [32] shows our Hugoniot data is consistent with their 65% and 85% dense CaF_2 data. Experimental details, a list of shots, and Hugoniot data are in [20].

XRD and analysis of the shock event.—Figures 3(a) and 3(b) show dynamic XRD data, measured as a function of time and, hence, shock state. Details of the experiments are in [20]. Static compression data [Fig. 3(c)] will be addressed later. Starting at $t = 0$, a planar shock wave traverses the sample and produces the maximum stress state ("state 1" later used in the stress-unit cell volume analysis). When the shock reaches the lower-impedance TPX, a release wave is generated traveling back into the CaF_2, lowering the stress state. When the initial shock reaches the TPX free surface, a release fan travels back through the window. Later the sample experiences multiple wave interactions, generating complex stress gradients and obscuring the stress state (Fig. 2 and Fig. S7 in [20]).

Depending on the shock stress, CaF_2 responds in different fashions. Figure 3(a) shows the dynamic XRD data for CaF_2 shock compressed to a maximum stress of 7.8 GPa. At 105 ns after impact, the shock wave has traveled through 30% of the sample. The cubic lattice is compressed, as indicated by the diffraction lines moving towards lower d spacings, meaning increased density. The shifted diffraction lines appear as shoulders on the right of ambient lines, because the x-ray beam is passing through both shocked and unshocked regions in CaF_2. By 259 ns the shock wave has made it through 90% of the sample, with only 10% still at ambient pressure. At 412 ns and 566 ns, as the stress continues to decrease because of release waves, the diffraction lines move back towards higher d spacings, meaning lower densities. Hence, the evolution of density (diffraction lines) mirrors the shock event unfolding in the sample. Line broadening is attributed to measurement over multiple stress states.

Shock-driven phase transition.—Figure 3(b) shows the unfolding of the CaF_2 fluorite to cotunnite phase transition under shock compression to 22.6 GPa. The sample starts in its fluorite structure (XRD-0). The phase transition to cotunnite initially appears in coexistence with the fluorite phase, as the shock wave creates a stress state of 22.6 GPa, while in front of the wave ~60% of the sample is still at 0 GPa (XRD-1). Next, the cotunnite phase becomes more prevalent (XRD-2, 216 ns), with ~25% of the sample between 10.5 and 22.6 GPa, and ~75% of the sample at 10.5 GPa, because of the impedance mismatch between the CaF_2 and TPX window [20]. At this time, both fluorite and cotunnite are visible, but the fluorite phase is compressed. At 370 ns (XRD-3) the sample is at 12.5 ± 1 GPa and is mostly in the cotunnite structure. At 523 ns CaF_2 reverts to a fluorite-cotunnite coexistence, as the shock state releases down to between 6 and 1 GPa. The shock stress necessary to induce the phase transition can be bound between 7.8 GPa and 22.6 GPa.

XRD and quantitative analysis.—Rietveld full-profile structural refinements [34] were done to confirm the phase

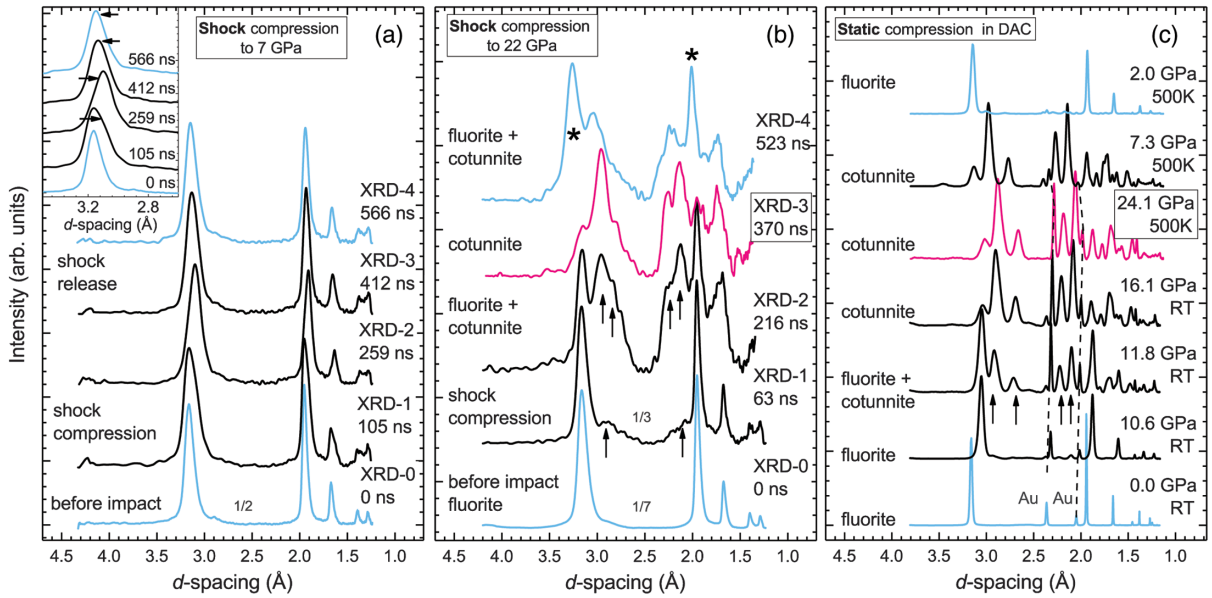

FIG. 3. *In situ* XRD patterns under shock compression measured as a function of time, showing (a) a shot to 7.8 GPa, below the phase transition conditions, (b) a shot to 22.6 GPa, with a phase transition, and (c) *in situ* XRD patterns under static compression in a diamond anvil cell (DAC) as a function of pressure and temperature. Times are relative to impact ($t = 0$). Inset in (a) shows a zoom of the [111] diffraction line, where shock compression and release are seen in the evolution of line position. In (b) arrows indicate new lines of the cotunnite phase; stars indicate the reappearing fluorite phase upon shock release. Fractions refer to intensity scaling done for display purposes. In (c) "Au" marks diffraction lines of the gold pressure calibrant and "RT" stands for room temperature.

composition in each time-dependent XRD snapshot. At ambient conditions CaF_2 starts in the fluorite structure ($Fm\bar{3}m$, $Z = 4$), which is built of a cubic close-packed array of cations, with anions occupying tetrahedral sites (Fig. 4).

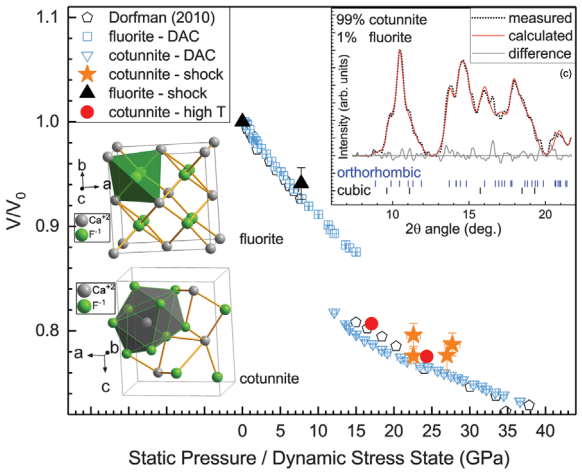

FIG. 4. The evolution of the CaF_2 unit cell volume versus stress/pressure obtained from dynamic (shock) and from static compression (DAC). Solid triangles and stars represent the fluorite and cotunnite unit cell volume, respectively, under shock compression. Open squares and inverted triangles refer to static compression at 298 K to 36 GPa in nonhydrostatic conditions. Solid red circles represent compression at 500 K. Open pentagons are from Ref. [10]. The inset on the right shows a Rietveld structural refinement at 370 ns, of the shock-driven phase transition from fluorite to cotunnite.

Upon shock compression to 22.6 GPa we observe the progressive development of the orthorhombic cotunnite-type structure ($Pnam$, $Z = 4$). A Rietveld refinement of diffraction pattern XRD-3 (Fig. 4) confirms that, at 370 ns, CaF_2 fully transitions to the cotunnite structure, where anions are in a distorted hexagonal-close-packed lattice, while cations are situated within tricapped trigonal prisms, with the three outer anions in the plane of the cation [35]. We estimate [20] that at 370 ns the stress state in the sample is predominantly uniform at 12.5 ± 1 GPa, with only 10% of the back of the target experiencing a gradient between 12 and 10 GPa.

Unit cell volumes were obtained from measured XRD patterns (not the Hugoniot state determined via impedance matching). Unit cell volume was evaluated from Rietveld full-profile structural refinements of patterns labeled XRD-1 for each shot, while the sample was in the well-defined initial shock state (Fig. 4 and [20]).

Dynamic vs static compression.—CaF_2 was also investigated under static compression at both ambient temperature and at 500 K with *in situ* XRD [Fig. 3(c)], under conditions designed to approximate the stress and temperature states achieved in our shock experiments. Synchrotron powder XRD in a DAC was carried out at end station 16-ID-B, HPCAT, of the Advanced Photon Source [20]. A comparison of diffraction results under shock compression with static compression reveals similarities and differences (Figs. 3 and 4). CaF_2 undergoes the same phase transition under both dynamic and static compression. A decrease in unit cell volume at the phase transition in both types of compression is a signature of a

first-order reconstructive transition. In Figs. 3(b) and 3(c) the pattern at 370 ns (shock compression) and that at 24.1 GPa, 500 K (static compression) have the same overall shape. Shock compression below or above the phase transition is characterized by a decrease in intensity and line broadening (Fig. 3). This is because there are two or more stress states during shock compression (decrease by a factor of 2 or 3) and because the transition is from a highly symmetric structure to a lower symmetry one (decrease by a factor of 3).

Dynamic compression is accompanied by shock-induced heating. For a single crystal of CaF_2 we estimate the shock temperatures to be 360 K at 7.7 GPa and 1000 K at 33.1 GPa. Heating effects are larger in a porous sample [36]. Evidence of heating is observed (Fig. 4) in the evolution of unit cell volumes versus stress (shock) and versus pressure (static compression). At equivalent pressure or stress states, the shocked sample has a larger unit cell volume (between 0.5% and 2%). This departure from static (cold) compression grows with increased shock of compression, because shock-induced heating becomes more significant as the stress state increases.

Kinetics of the phase transition.—Plate-impact, shock-compression experiments provide a short, steady shock wave, without spatial stress gradients as the shock wave traverses the sample for the first time (state 1). For the experiment shown in Fig. 3(b), the initial shock transit is ~146 ns. Thus, if the phase transition were instantaneous, only the cotunnite phase would exist in the diffraction pattern at 216 ns (XRD-2). Instead, we still observe a compressed fluorite-cotunnite mixture, although the pressure throughout the sample is greater than the transition threshold pressure. Not until ~370 ns (XRD-3), where a nearly steady stress state exists, with 90% of the sample at 12.5 ± 1 GPa (Fig. 4 and [20]), do we observe a nearly complete transition to the cotunnite structure.

Our experiments under static compression show the coexistence of phases over a range of pressures between 11 and 16 GPa in CaF_2 and point to a sluggish phase transition driven by diffusion, consistent with Yel'kin *et al.* [12]. Upon decompression, both the shock and the static compression-driven transitions show significant hysteresis. Under static compression, upon decrease of pressure from 24 GPa at 500 K the transition is found to be completely reversible, but not until 2 GPa [Fig. 3(c)]. Under shock compression, at 523 ns, the stress distribution in the sample is between 6 and 1 GPa [20]. In the corresponding XRD pattern, we observe a reversibility to fluorite, although with significant coexistence of the cotunnite phase below 7.8 GPa, which is the estimated lower bound of the phase transformation. At such a late time, edge effects are likely affecting the sample, especially along the angled path of the x-ray beam.

Static compression and shock-driven phase transitions, especially of first order, are usually of a mixed type, with essentially unexplored kinetics. The results of our *in situ* XRD experiments on CaF_2 and analysis of phase percentages from Rietveld refinements allow us to analyze quantitatively phase transition kinetics under shock compression by using the classical formulation of nucleation, developed independently by Kolmogorov [37], Johnson and Mehl [38], and Avrami [39–41] (KJMA), but applied to processes in the nanosecond time scale [20].

We describe the volume fraction of the cotunnite phase $\alpha(t)$ formed in the process of a shock-driven transition, during time t using the KJMA model,

$$\alpha(t) = 1 - \exp\{-[k(t-\tau)]^N\}. \quad (1)$$

The Avrami parameter, N, is indicative of heterogeneous or homogeneous nucleation and changes from 0.3 to 4, depending on growth mechanisms. τ is the transition incubation time and k is the crystallization rate constant. We note that the applicability of the KJMA formalism for quantification of polymorphic transitions under shock compression with an abrupt volume change must be approached carefully, since the formalism was developed for transformations between isotropic phases with a small volume jump and a zero shear modulus. In our analysis, we group the shots to stresses between 22 and 27 GPa as a first approximation that only considers stress as being sufficient to induce the phase transitions, because the temperature difference between those stresses is small. While an imperfect approach, it nonetheless provides insight into the kinetics of the fluorite-cotunnite phase transition.

Figure 5 shows the phase concentration data and various KJMA fits. The best fit to our data results in $\tau = 36.3$ ns, $N = 0.19$, and $k = 2.9 \times 10^{-4}$. This fit suggests a phase transition characterized by an incubation time $\tau \sim 36 \pm 1$ ns [20]. This is consistent with the transition delay hinted at in a visual inspection of our time-dependent XRD patterns (Fig. 3). The incubation time, along with the hysteresis on stress release, suggests a first-order

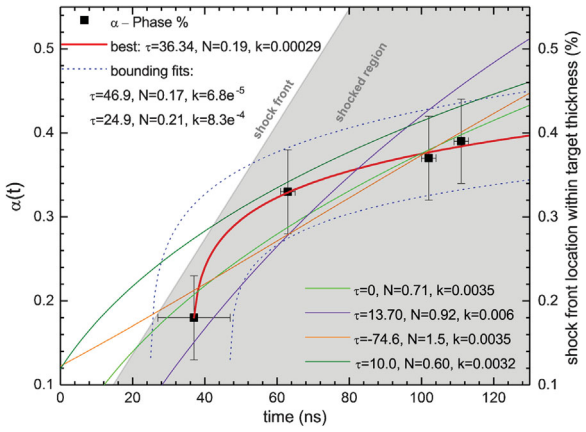

FIG. 5. Phase percentage versus time. The phase transition lags behind the shock front, marked with a grey line. The colored lines are various fits to the data using the KJMA formalism of Eq. (1).

reconstructive transition and points to a kinetic barrier that impedes the transition at the equilibrium pressure of the two phases. The incubation time is comparable with shock compression of various materials, from 6 ns to tens of ns [4,42]. Figure 5 shows that the phase transformation rate is initially fast, but slows when the cotunnite phase percentage reaches ~30%. Under static compression, Yel'kin *et al.* [12] observed a similar slowdown in the transition rate around $\alpha \sim 20\%$–30%.

Our fitted $N = 0.19 \pm 0.04$ [20] indicates an inhomogeneous distribution of nucleation sites [43] and points to a distribution of grain sizes, where transformation begins on the surface of grains. It was found that heterogeneous nucleation and likely simultaneous diffusion-controlled crystallization correspond to $N \leq 1$ [44]. Our Avrami parameter is also consistent with $N \sim 0.1$ found under static compression [12] for the stage when more than ~20–30% cotunnite is formed. Forcing $N > 1$ produces negative incubation times (see [20]). Using molecular dynamics simulations, Boulfelfel *et al.* [45] showed that the pressure-induced transition in CaF_2 is characterized by nucleation and growth of the new phase, with local melting of the fluoride sublattice (which produces defects), followed by recrystallization into the cotunnite structure. Our results are consistent both with local melting (long incubation time) and with heterogeneous nucleation and growth processes (low Avrami parameter).

We demonstrated a shock-driven phase transition in an ionic solid, on nanosecond time scales and at a microstructural level, from a more-ordered to a less-ordered structure. Time-resolved XRD illustrates the unfolding of the reconstructive phase transition and hysteresis on unloading. A direct comparison of unit cell volumes between dynamic and static loading points to measurable structural effects of temperature on increased shock loading. The ability to combine *in situ* XRD measurements with well-characterized shock loading experiments now allows for Rietveld, full-profile structural refinements that lead to analysis of the phase concentrations. Our results give insight into the kinetic time scale of the fluorite-cotunnite phase transition under shock compression, which is relevant to a number of isomorphic compounds. These methods and results can be used to develop improved kinetic models for complex, solid-solid phase transitions.

The authors are grateful to Dr. Thomas Mattsson of SNL for a critical reading of the manuscript and valuable advice. We also thank the two anonymous reviewers whose comments greatly improved the Letter. The authors thank P. Rigg and the DCS team, N. Cofer, J. Usher, K. Hodge and R. Hickman of SNL, S. Payne of NSTEC, as well as E. Rod and the HPCAT team. Sandia National Laboratories is a multimission laboratory managed and operated by National Technology and Engineering Solutions of Sandia, LLC., a wholly owned subsidiary of Honeywell International, Inc., for the U.S. Department of Energy's National Nuclear Security Administration under Contract No. DE-NA-0003525. A portion of this publication is based upon work performed at the Dynamic Compression Sector, which is operated by Washington State University under the U.S. Department of Energy (DOE)/National Nuclear Security Administration Award No. DE-NA0002442. Portions of this work were performed at HPCAT (Sector 16), Advanced Photon Source (APS), Argonne National Laboratory. HPCAT operations are supported by DOE-NNSA under Award No. DE-NA0001974, with partial instrumentation funding by NSF. J. S. and S. S. acknowledge the support of DOE-BES/DMSE under Award No. DE-FG02-99ER45775. The Advanced Photon Source is a U.S. Department of Energy (DOE) Office of Science User Facility operated for the DOE Office of Science by Argonne National Laboratory under Contract No. DE-AC02-06CH11357. Work at HiPSEC is supported by the National Nuclear Security Administration under the Stewardship Science Academic Alliances program through DOE Cooperative Agreement No. DE-NA0001982.

*pekalit@sandia.gov

[1] D. Milathianaki, S. Boutet, G. J. Williams, A. Higginbotham, D. Ratner, A. E. Gleason, M. Messerschmidt, M. M. Seibert, D. C. Swift, P. Hering, J. Robinson, W. E. White, and J. S. Wark, Science **342**, 220 (2013).
[2] A. Higginbotham, P. G. Stubley, A. J. Comley, J. H. Eggert, J. M. Foster, D. H. Kalantar, D. McGonegle, S. Patel, L. J. Peacock, S. D. Rothman, R. F. Smith, M. J. Suggit, and J. S. Wark, Sci. Rep. **6** 24211 (2016).
[3] S. J. Turneaure, N. Sinclair, and Y. M. Gupta, Phys. Rev. Lett. **117**, 045502 (2016).
[4] A. E. Gleason, C. A. Bolme, E. Galtier, H. J. Lee, E. Granados, D. H. Dolan, C. T. Seagle, T. Ao, S. Ali, A. Lazicki, D. Swift, P. Celliers, and W. L. Mao, Phys. Rev. Lett. **119**, 025701 (2017).
[5] K. F. Seifert, Berich. Bunsen. Gesell. **70**, 1041 (1966).
[6] D. Dandekar and J. Jamieson, Trans. Am. Crystallogr. Assoc. (1965-1995) **5**, 19 (1969).
[7] L. Gerward, J. S. Olsen, S. Steenstrup, M. Malinowski, S. Asbrink, and A. Waskowska, J. Appl. Crystallogr. **25**, 578 (1992).
[8] X. Wu, S. Qin, and Z. Wu, Phys. Rev. B **73**, 134103 (2006).
[9] H. Shi, W. Luo, B. Johansson, and R. Ahujia, J. Phys. Condens. Matter **21**, 415501 (2009).
[10] S. M. Dorfman, F. Jiang, Z. Mao, A. Kubo, Y. Meng, V. B. Prakapenka, and T. S. Duffy, Phys. Rev. B **81**, 174121 (2010).
[11] J. R. Nelson, R. J. Needs, and C. J. Pickard, Phys. Rev. B **95**, 054118 (2017).
[12] F. S. Yel'kin, O. B. Tsiok, V. V. Brazhkin, and L. G. Khvostantsev, Phys. Rev. B **73**, 094113 (2006).
[13] A. Kavner, Phys. Rev. B **77**, 224102 (2008).
[14] G. A. Adadurov, Z. G. Aliyev, L. O. Atovmyan, Y. G. Borod'ko, O. N. Breusov, A. N. Dremin, A. K. Muranevich, and N. P. Khrameyeva, Izv. Akad. Nauk SSSR, Neorg. Mater. **3**, 6 (1965).
[15] V. N. German, N. N. Orlova, M. N. Pavlovskii, L. A. Tarasova, and R. F. Trunin, Izv. Akad. Nauk SSSR, Fiz. Zemli **8**, 12 (1975).

[16] M. Hasegawa, K. Kondo, and A. Sawaoka, Jpn. J. Appl. Phys. **23**, 20 (1984).
[17] T. Sekine and T. Kobayashi, Phys. Chem. Miner. **38**, 305 (2011).
[18] W. Carter and S. Marsh, Technical Report No. LA-13006-MS, Los Alamos National Laboratory, 1995.
[19] S. Root, T. R. Mattsson, K. Cochrane, R. W. Lemke, and M. D. Knudson, J. Appl. Phys. **118**, 205901 (2015).
[20] See Supplemental Material at http://link.aps.org/supplemental/10.1103/PhysRevLett.119.255701, which includes additional experimental details and results for dynamic and static compression experiments, methods for estimating stress distribution in targets, and results of Rietveld structural refinements, and also includes Refs. [18,21–30].
[21] O. T. Strand, D. R. Goosman, C. Martinez, T. L. Whitworth, and W. W. Kuhlow, Rev. Sci. Instrum. **77**, 083108 (2006).
[22] S. Root, L. Shulenburger, R. W. Lemke, D. H. Dolan, T. R. Mattsson, and M. P. Desjarlais, Phys. Rev. Lett. **115**, 198501 (2015).
[23] T. Ao and D. H. Dolan, Technical Report No. SAND2010-3628, Sandia National Laboratories, 2010.
[24] C. Prescher and V. B. Prakapenka, High Press. Res. **35**, 223 (2015).
[25] O. L. Anderson, D. G. Isaak, and S. Yamamoto, J. Appl. Phys. **65**, 1534 (1989).
[26] J. M. McGlaun, S. L. Thompson, and M. G. Elrick, Int. J. Impact Eng. **10**, 351 (1990).
[27] W. Herrmann, J. Appl. Phys. **40**, 2490 (1969).
[28] M. Carroll and A. C. Holt, J. Appl. Phys. **43**, 759 (1972).
[29] G. R. Johnson and W. H. Cook, *Proceedings of the Seventh International Symposium on Ballistics, The Hague, The Netherlands, 1983* (1983), pp. 541–547.
[30] G. R. Johnson and W. H. Cook, Eng. Fract. Mech. **21**, 31 (1985).
[31] G. E. Duvall and R. A. Graham, Rev. Mod. Phys. **49**, 523 (1977).
[32] T. Taniguchi, K. Kondo, and A. Sawaoka, J. Appl. Phys. **61**, 196 (1987).
[33] L. V. Al'tshuler, M. A. Podurets, G. V. Simakov, and R. F. Trunin, Fiz. Tverd. Tela **15**, 1436 (1973) [Sov. Phys. Solid State **15**, 969 (1973)].
[34] H. M. Rietveld, J. Appl. Crystallogr. **2**, 65 (1969).
[35] E. Morris, T. Groy, and K. Leinenweber, J. Phys. Chem. Solids **62**, 1117 (2001).
[36] G. Fenton, D. Grady, and T. Vogler, J. Dyn. Behav. Mater. **1**, 103 (2015).
[37] A. Kolmogorov, Bull. Russ. Acad. Sci.: Phys. **3**, 555 (1937).
[38] W. Johnson and R. Mehl, Trans. Am. Inst. Min., Metall. Pet. Eng. **135**, 416 (1939).
[39] M. Avrami, J. Chem. Phys. **7**, 1103 (1939).
[40] M. Avrami, J. Chem. Phys. **8**, 212 (1940).
[41] M. Avrami, J. Chem. Phys. **9**, 177 (1941).
[42] K. Ichiyanagi and K. G. Nakamura, Metals **6**, 17 (2016).
[43] N. X. Sun, X. D. Liu, and K. Lu, Scr. Mater. **34**, 1201 (1996).
[44] J. A. Lopes-Da-Silva and J. A. P. Coutinho, Energy Fuels **21**, 3612 (2007).
[45] S. E. Boulfelfel, D. Zahn, O. Hochrein, Y. Grin, and S. Leoni, Phys. Rev. B **74**, 094106 (2006).